Kepler Orbits in Pairs of Disks Settling in a Viscous Fluid

Rahul Chajwa,[1] Narayanan Menon,[2] and Sriram Ramaswamy[3,4]
[1]International Centre for Theoretical Sciences, Tata Institute of Fundamental Research, Bengaluru 560 089, India
[2]Department of Physics, University of Massachusetts, Amherst, Massachusetts 01003, USA
[3]Centre for Condensed Matter Theory, Department of Physics, Indian Institute of Science, Bengaluru 560 012, India
[4]TIFR Centre for Interdisciplinary Sciences, Hyderabad 500 107, India

(Received 7 May 2018; published 4 June 2019)

We show experimentally that a pair of disks settling at negligible Reynolds number ($\sim 10^{-4}$) displays two classes of bound periodic orbits, each with transitions to scattering states. We account for these dynamics, at leading far-field order, through an effective Hamiltonian in which gravitational driving endows orientation with the properties of momentum. This treatment is successfully compared against the measured properties of orbits and critical parameters of transitions between types of orbits. We demonstrate a precise correspondence with the Kepler problem of planetary motion for a wide range of initial conditions, find and account for a family of orbits with no Keplerian analog, and highlight the role of orientation as momentum in the many-disk problem.

DOI: 10.1103/PhysRevLett.122.224501

Collective gravitational settling in a viscous fluid is a notoriously challenging problem in the physics of driven systems with long-range interactions. In the Stokesian limit of Reynolds number $\mathrm{Re} \to 0$, sedimenting particles, which are monopoles of force density, manifest the hydrodynamic interaction [1–4] in its strongest form [5,6]. Among the consequences of this strong coupling are chaos in three-particle settling [7,8] and the resulting statistical character of many-particle sedimentation [6,9–11]. Interestingly, however, the collective settling of identical spheres can be built up from two-particle processes [12–14]. A pair falls faster than an isolated sphere, with a horizontal drift when their separation is oblique to gravity, but a constant separation vector thanks to the reversibility of Stokes flow [2]. By the same token a single apolar axisymmetric particle falls without rotating, drifting horizontally at a rate proportional to its constant tilt. However, for two sedimenting disks a rich phase-space dynamics emerges, via mutual rotation due to a coupling between orientational and translational degrees of freedom [15–18].

In this Letter, we present experiments that classify the possible dynamical behaviors of a settling pair of disks. We show that a symmetry-based far-field theory, without a detailed calculation of the mutual rotation coupling, accounts for the dynamics through the emergence of an effective Hamiltonian for this wholly dissipative system. Horizontal position and tilt in the presence of gravity thus precisely mimic coordinate and momentum, with an inherited time-reversal invariance. This emergent canonical dynamics persists in the many-disk problem, where it competes with the well-known velocity-fluctuations problem [6,11,19–21] in the sedimentation of isotropic particles.

Our experiments are conducted on pairs of identical disks, falling in viscous fluid ($\mathrm{Re} \sim 10^{-4}$) in a quasi-two-dimensional container with dimensions of $30 \times 50 \times 5$ cm (width × height × depth). The fluid was transparent polydimethylsiloxane (silicone oil) of viscosity 60 000 cSt and density 0.96 g cm^{-3}. The disks, of radius $a = 0.6$ cm, and 1 mm thickness, are made of aluminum (density 2.7 g cm^{-3}), sanded smooth, and spray-painted black. Their settling dynamics are captured every 5 seconds with a NikonD700 DLSR camera. The images were converted to 8-bit and thresholded after subtracting the background. Tracking was done by fitting an ellipse to the disks, with the centroid of the ellipse giving the positions (x_i, y_i) with an error of $\pm 0.02a$ and orientation of the major axis giving θ_i of the disks with an error of $\pm 0.06°$.

As shown in Fig. 1, the trajectories of the centers of the disks lie in a plane. Assuming translation symmetry in the x-y plane, and taking advantage of the observation that there are no rotations due to torques about the x and y axes, the six coupled degrees of freedom can be reduced to two separation and two orientation degrees of freedom. Our observations suggest two qualitatively distinct trajectory types: scattering, in which the separation increases monotonically, and bound, in which separation and orientations oscillate with a characteristic amplitude and wavelength. The oscillatory behavior further falls into two classes, to be discussed later.

We ask the following: (i) Is there a well-defined boundary in the space of initial conditions that separates periodic and scattering (i.e., infinite wavelength) behavior, or do our "scattering" states simply have a wavelength longer than the container height? (ii) What determines the emergent time period and wavelength of the periodic orbits?

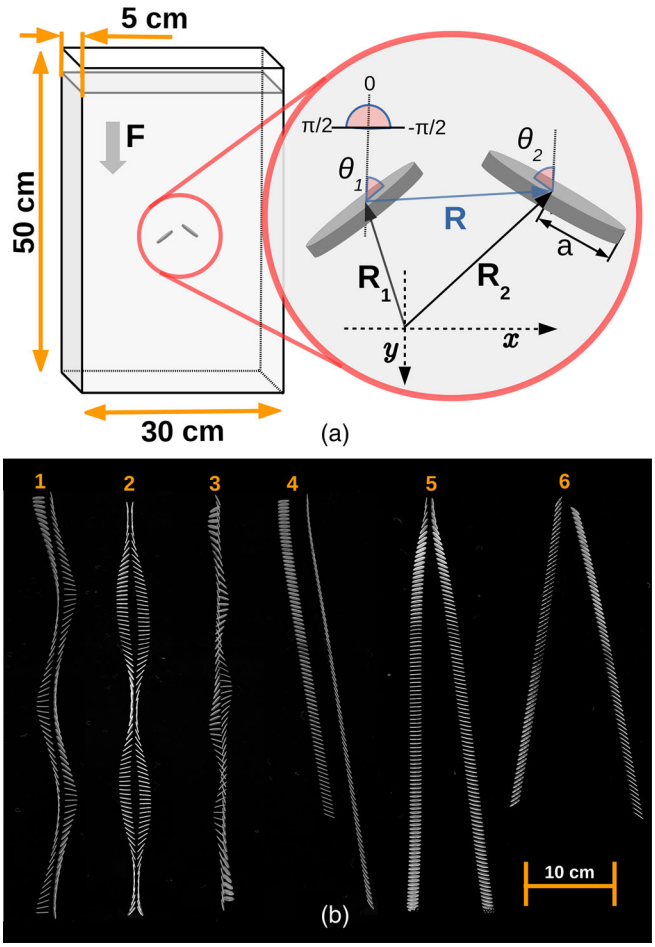

FIG. 1. Bound and scattering behavior: (a) Quasi-two-dimensional setup, prepared with disk normal and separation vector $\vec{R} = \vec{R}_2 - \vec{R}_1$ in plane of settling geometry, (x, y). Disk orientation angles θ_1 and θ_2 measured wrt gravity pointing along the $\hat{y}$ direction. (b) Time lapse showing observed pair dynamics generated by varying initial interdisk separation (x_0, y_0) and orientations θ_1, θ_2. Trajectories fall into two broad classes: periodic bound (1–3) and scattering (4–6).

Within the four-dimensional space of initial separations and orientations, it is convenient to work with $x \equiv x_2 - x_1$, $y \equiv y_2 - y_1$, $\theta^- \equiv \theta_2 - \theta_1$, and $\theta^+ \equiv \theta_1 + \theta_2$. Here, θ_i is measured with respect to y axis, defined to be $-$ve in first and fourth quadrants and $+$ve in second and third quadrants (Fig. 1). We begin with the symmetric case with initial $\theta_1 = -\theta_2$ and $y = 0$. The resulting trajectories [Fig. 2(a)] are symmetric, i.e., $\theta^+ = 0$ at all times. For small initial value x_0 of the horizontal separation x, the θ_i undergo full rotations and x oscillates periodically, as observed in experiments and simulations by Jung *et al.* [16]. As x_0 is increased the wavelength and amplitude of the oscillations increase sharply [Fig. 2(d)], until the terminal motion seems to approach the linear trajectories of isolated Stokesian disks (see the Supplemental Material [22], Video 1). Finite container height makes it impossible to establish experimentally the existence of a threshold value of x_0 at which the wavelength and amplitude actually diverge. A similar limitation applies to the numerical evidence for scattering orbits [23] using an expansion in a/R and the method of reflections [2,3].

Working at leading order in a/R, we construct an effective Hamiltonian approach to the disk-settling problem and map the symmetric case to the gravitational Kepler problem, thus establishing the transition between periodic and scattering orbits. We then go on to explain the behaviors seen in asymmetric settling. We begin with an isolated settling disk: the horizontal velocity of an isolated settling disk is $\dot{x_1} = F\alpha \sin 2\theta_1$, where F is its buoyant weight and the mobility α is defined below. The tilt angle θ_1 remains constant. We can thus view the trivial evolution of x_1 and θ_1 as the Hamiltonian dynamics of a free particle with momentum θ_1 and kinetic energy proportional to $\cos 2\theta_1$. This approach also applies to the two-disk case, where θ_1, θ_2 do not remain constant.

For symmetric settling, retaining the lowest nonvanishing contribution in an expansion (see the Supplemental Material [22], text) in a/x, $\dot{x} = 2F\alpha \sin\theta^-$ and $\dot{\theta^-} = 2F\gamma/x^2$. The proportionality constants α and γ are determined by the solution for an isolated settling spheroid [24,26]. The mobility $\alpha = -({X_A}^{-1} - {Y_A}^{-1})/12\pi\mu a$ and $\gamma = 1/8\pi\mu$, where the resistance functions $X_A = 8/3\pi$ and $Y_A = 16/9\pi$ [3] in the limiting case of $e = \sqrt{1 - b^2/a^2} \to 1$ for radius a and thickness b of the disk. The above far-field equations can be recast as Hamiltonian dynamics $\dot{x} = \partial_{\theta^-}\mathcal{H}, \dot{\theta^-} = -\partial_x\mathcal{H}$ with

$$\mathcal{H} \equiv 4F\alpha \sin^2\frac{\theta^-}{2} + 2F\gamma/x, \tag{1}$$

where $4F\alpha\sin^2(\theta^-/2)$ and $2F\gamma/x$ play the roles of kinetic and potential energy, respectively, but the $1/x$ comes from the viscous hydrodynamic kernel, not gravity. This is precisely the reduced Hamiltonian for the Kepler problem [25] when expressed in terms of azimuthal angle θ^- and radial coordinate x [Fig. 2(b)]. The solution

$$\frac{1}{x} - \frac{1}{x_0} = \frac{\alpha}{\gamma}(\cos\theta^- - \cos\theta_0^-), \tag{2}$$

to the equations of motion, obtained earlier by Kim [23] for far-field scattering trajectories, is simply conservation of $\mathcal{H}$, describing both bound and scattering orbits [see Fig. 2(c)], with a transition as $x_0 \to x_c = 4a/\pi$. Note that the observed amplitude diverges at $x_c = 1.02a$ which is smaller than $4a/\pi$ [see Fig. 2(d)]. A circular Kepler orbit arises only for $\alpha = 0$, which is the case of a pair of identical spheres. Given the very close approach of the disks in a bound state, the far-field mapping to the Kepler problem bears up surprisingly well against experimental observations, as detailed in Fig. 2.

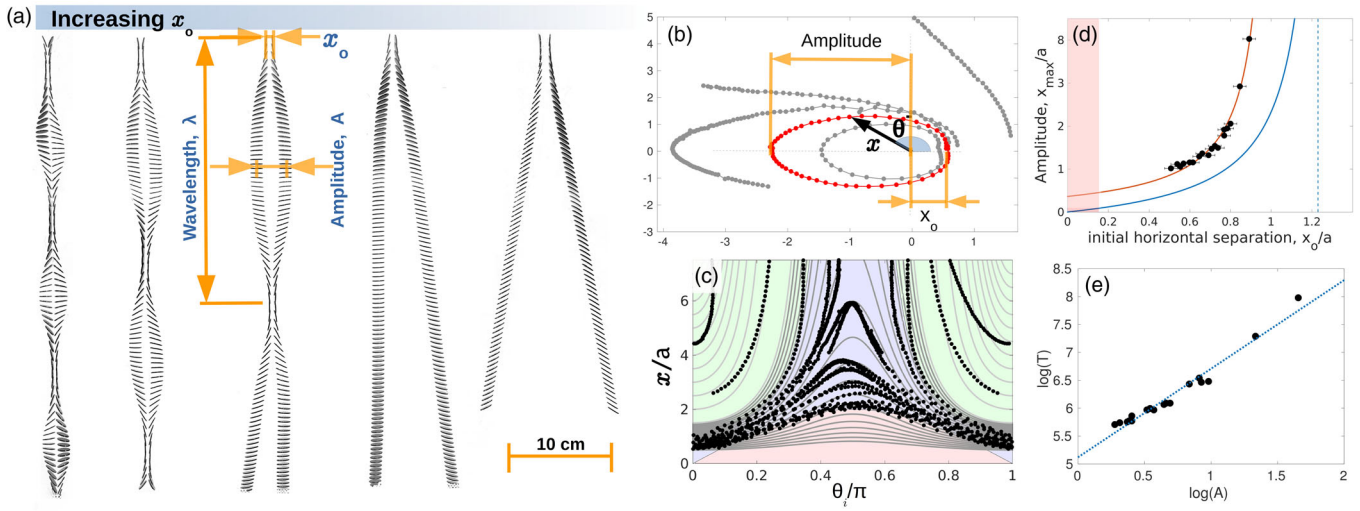

FIG. 2. Symmetric settling: (a) Experimental time-lapse images showing transition from periodic to scattering trajectories with increasing x_0. Wavelength λ and amplitude A appear to diverge as x_0 approaches a critical value. (b) Elliptical Kepler orbits for the bound states are clearly seen when the measured x and θ^- are displayed as radial and azimuthal coordinates, respectively. (c) Trajectories in x-θ_i plane, $i = 1, 2$, showing regions of bound and scattering trajectories. The gray curves are predicted by the far-field analysis $1/x = 1/x_0 + (\pi/8a)(\cos 2\theta_i - \cos 2\theta_{i0})$, where θ_{i0}, x_0 are the initial values. Red, blue, and green represent restricted, bound, and scattering regions, respectively. (d) Amplitude vs minimum separation fits $1/(x_0^{-1} - x_c^{-1}) + c$ with $x_c = 1.02a$ and $c = 0.725a$ (red curve), qualitatively consistent with the asymptotic far-field prediction (blue) $1/(x_0^{-1} - \pi/4a)$. (e) Scaling of period T with amplitude A, $T \sim A^\nu$, with $\nu \simeq 1.59 \pm 0.11$ consistent with the $3/2$ of Kepler's third Law.

A simple case of asymmetric initial conditions consists of releasing the disks at the same height with their normal vectors perpendicular to each other, $\theta^+ = \pi/2$ [Figs. 3(a)–3(c)]. Once again, periodic dynamics in the orientation is observed, with the added complexity of y oscillating between positive and negative values, and an apparent transition to unbounded orbits with increasing x_0.

The effective Hamiltonian description above provides a useful framework for understanding the dynamics resulting from a more general set of initial conditions $(x_0, y_0, \theta^+, \theta_0^-)$. A reduction to an effective two-dimensional dynamics can be achieved for asymmetric initial conditions $\theta_0^+ \neq 0$ as well, and periodic behavior is preserved but more complex [Figs. 3 and 4]. The resulting non-Keplerian behavior can be understood by extending Eq. (1) to incorporate the dependence of the angular velocity of the disks on the angle between the separation vector $\mathbf{R}$ and the external force $\mathbf{F}$. To leading order in a/R, the angular velocities of disks are equal and opposite, $\dot{\theta}_1 = -\dot{\theta}_2 = \gamma \mathbf{F} \times \mathbf{R}/R^3$. With this additional ingredient, we get the general equations of motion

$$\dot{x} = 2F\alpha \sin\theta^- \cos\theta^+, \qquad \dot{y} = -2F\alpha \sin\theta^- \sin\theta^+ \tag{3}$$

$$\dot{\theta^-} = 2F\gamma \frac{x}{R^3}, \qquad \dot{\theta^+} = 0. \tag{4}$$

Here α and γ are same as before Eq. (1). The form (3) and (4) also follows on general grounds of symmetry (see the Supplemental Material [22], text). The conservation of θ^+ in Eq. (4) constrains the dynamics of x and y to a line with slope $-\tan\theta^+$, reducing the number of variables to two, thus allowing phase plane analysis. The dynamics in terms of $S \equiv |\mathbf{R} - \mathbf{R}_0|$ and θ^- (see the Supplemental Material [22], text) is given by $\dot{S} = \partial_{\theta^-}\mathcal{H}, \dot{\theta^-} = -\partial_S \mathcal{H}$, with effective Hamiltonian

$$\mathcal{H} \equiv 4F\alpha \sin^2\frac{\theta^-}{2} + 2F\frac{\bar{\gamma}(S)}{R(S)}, \tag{5}$$

where $\bar{\gamma}(S) \equiv \gamma(y_0 - S\sin\theta^+)/(y_0\cos\theta^+ + x_0\sin\theta^+)$ and $R(S) = (S^2 + {R_0}^2 + 2Sx_0\cos\theta^+ + 2Sy_0\sin\theta^+)^{1/2}$. Note that, in the limit $\theta^+ \to 0$, Kepler orbits are realized for more general initial separations with $y_0 \neq 0$.

The Hamiltonian (5) for $\theta^+ = \pi/2$ implies a dynamics with y oscillating between positive and negative values given by $y = \pm x_0 \cos\theta^- / \sqrt{(8a/\pi x_0)^2 - \cos^2\theta^-}$, constant x, and, with increasing x_0, a transition from periodic to unbound orbits at $x_c = 8a/\pi$ (see the Supplemental Material [22], text). These are in accord with observations (see Fig. 3 and the Supplemental Material [22], Video 2), though the experiments additionally show small oscillations in x possibly arising from near-field effects and small imprecision in initial release angles.

For both symmetric and perpendicular initial conditions, the time period diverges at the boundary between bound and scattering orbits. Assuming disk thickness $\ll$ radius, we have two length scales in the problem: the radius a of the disk and the separation R between the particles. One expects the period $T = (a^2\mu/F) f(R/a, \mathrm{Re}, \mathrm{Fr}, \theta_0^+, \theta_0^-)$, where the

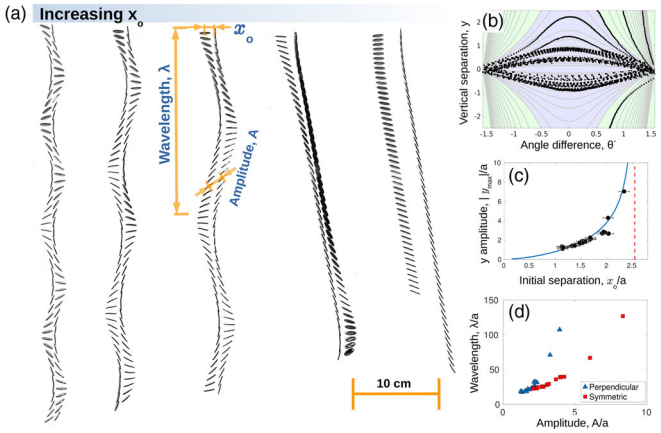

FIG. 3. Perpendicular initial condition. (a) Experimental time-lapse images, when the disks are released with perpendicular initial orientation. x_0 is increased from left to right leading to a divergence in vertical separation y. (b) Experimental trajectories in the θ^--y plane represented by points, compared with the far-field result plotted in gray solid lines: $y = \pm x_0 \cos\theta^- / \sqrt{(8a/\pi x_0)^2 - \cos^2\theta^-}$. Blue and green in the phase diagram represent bound and scattering regions, respectively, as predicted by far-field analysis. (c) Divergence of amplitude of y oscillations captured by plotting maximum value of y/a as function of x_0/a. Solid curve is far-field prediction of amplitude: $A(x_0) = x_0/\sqrt{(8a/\pi x_0)^2 - 1}$, with the red dotted line representing the critical $x_0 = 8a/\pi$. (d) Observed wavelength λ/a increases more strongly as function of amplitude A/a for perpendicular (blue) as compared to symmetric case (red).

scaling function f depends on the initial conditions, as well as on the Reynolds number $\mathrm{Re} = \rho U a/\mu \simeq 10^{-4}$ and Froude number $\mathrm{Fr} = U/\sqrt{ga} \simeq 10^{-3}$ both of which are negligibly small. $f(R_0/a)$ can be calculated for symmetric and perpendicular cases (see the Supplemental Material [22], text) in the far-field limit, whence we find that the wavelength $\lambda \sim TF/a\mu$ diverges more strongly ($\sim A^3$) for the perpendicular case than for the symmetric case ($\sim A^{3/2}$ Kepler's third Law), a trend consistent with our observations [see Fig. 3(d)].

Rocking—a qualitatively distinct periodic behavior analogous to libration in a pendulum, in which θ^- oscillates in a limited range—emerges for $\pi/2 < \theta^+ < \pi$ (see the Supplemental Material [22], Video 3). Releasing the disks with $\theta_1 = \pi/2$ and decreasing $-\theta_2$ from $\pi/2$ (symmetric case) toward zero we experimentally capture the tumbling-rocking transition at $\theta_0^- = -\pi/2$ [see Figs. 4(a) and 4(b)]. Unlike in tumbling, in rocking orbits the sign of x and hence, from Eq. (4), of $\dot{\theta}^-$, alternates as the particles interchange their relative horizontal positions. Except for the special cases of parallel and perpendicular release, rocking dynamics is best viewed in x, y, and θ^- space albeit with proportional x and y displacements. Figure 4(c) shows the trajectories projected on the x-θ^- plane. The tumbling-rocking transition can once again be understood in terms of the effective Hamiltonian (5) (see the Supplemental Material [22], text). The extension to the case of dissimilar disks is also discussed in the Supplemental Material [22].

The two-particle processes discussed above can be used as a building block to study the coupling of positions and orientations in multiple disks settling in our geometry [see Fig. 1], within the far-field description [10,13,20]. Let (x_m, y_m) be the position of the mth particle. At each location r_m, define $\vec{U}(r_m) \equiv \sum_{n\neq m}^{N} F\mathbb{G}_{xy}(r_m - r_n)\hat{x} + F\mathbb{G}_{yy}(r_m - r_n)\hat{y} + F\alpha\hat{y}$, where $\mathbb{G}_{ij}$ is the Oseen tensor [2,3] and m, n are particle labels. Pairwise addition of forces and torques at position r_m due to particles at other locations r_n gives the coupled dynamics of the mth disk

$$\dot{x}_m = F\alpha \sin 2\theta_m + U_x, \qquad \dot{y}_m = F\alpha \cos 2\theta_m + U_y \tag{6}$$

and

$$\dot{\theta}_m = -\frac{F\gamma}{2}\frac{\partial}{\partial x_m}\sum_{n\neq m}^{N}\frac{1}{\sqrt{(x_m - x_n)^2 + (y_m - y_n)^2}}. \tag{7}$$

From Eqs. (6) and (7), we can show (R. Chajwa *et al.*, unpublished) that the dynamics in the (x, θ) space can be viewed as an effective Hamiltonian dynamics riding on the y-averaged background flow, $\dot{x}_m = \partial_{\theta_m}\mathcal{H}^X + \bar{U}_x(x_m)$, $\dot{\theta}_m = -\partial_{x_m}\mathcal{H}^X$ where the effective Hamiltonian takes the form

$$\mathcal{H}^X \equiv \sum_{m=1}^{N} F\alpha \sin^2\theta_m - \sum_{n\neq m}^{N} F\gamma \int L(x_m - x_n)dx_m, \tag{8}$$

where the expressions for L and $\bar{U}_x$ can be obtained from the steady-state average of Eqs. (6) and (7) over the y coordinates. $\bar{U}_x$ contains the giant velocity fluctuations of [21] and possible screening mechanisms à la Refs. [6,11,19,20] and the "potential energy" term containing γ in Eq. (8) incorporates the tilt-induced lateral drift [10].

Our experiments have uncovered a rich dynamics in the zero-Reynolds-number settling of a pair of identical disks, with a well-defined boundary between bound and scattering orbits and two distinct classes of periodic bound-state motion. Despite limited accuracy in locating the bound-scattering boundary, and excluding extreme situations where a disk is in the hydrodynamic shadow of another (see the Supplemental Material [22], Video 4), the far-field hydrodynamic interaction offers a satisfactory and detailed understanding of the dynamics, even close to particle contact. It should be clear that our analysis is applicable to any uniaxial shape with fore-aft symmetry along the symmetry axis. Unexpectedly, the conservative dynamics generated by an effective Hamiltonian governs this viscosity-dominated system, with the tilt of the disks playing the role of momentum. For a large family of initial

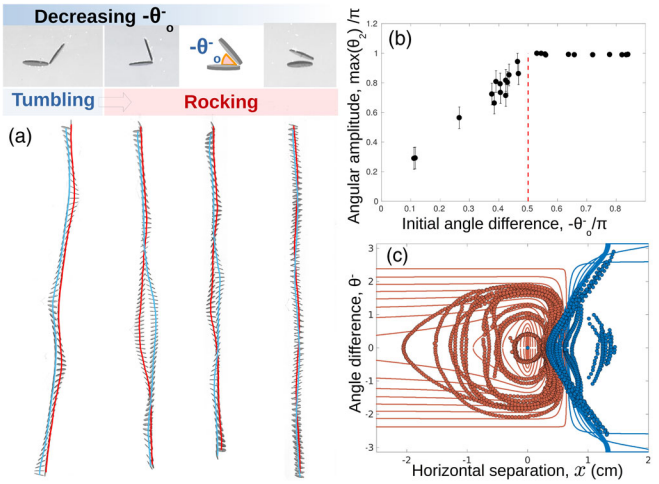

FIG. 4. Tumbling to rocking transition. (a) As θ_0^- decreases, tumbling gives way to rocking. Trajectory of disk on right (red) exchanges relative x position with that on left (blue) except for the first trajectory where $-\theta_0^- > \pi/2$. (b) Maximum angle of disk on right is plotted as function of $-\theta_0^-$, and rocking-tumbling transition observed at $\theta_0^- = -\pi/2$ (dotted red line), consistent with far-field calculation. (c) Trajectories plotted in x-θ^- plane; red symbols represent rocking motion and blue represents tumbling. The corresponding red and blue solid curves represent the far-field prediction of rocking and tumbling dynamics, respectively (see the Supplemental Material [22], text).

conditions, the problem maps precisely to that of Kepler orbits. We find and account for a distinct family of orbits with no planetary-orbit analogue, where the angle executes oscillations over a limited range. For the many-disk problem, a y-averaged treatment yields Hamiltonian dynamics for (x, θ) as conjugate variables, riding on a background carrying the velocity fluctuations of sedimenting spheres [6,11,19,20].

This work was begun when the authors were affiliated to the TIFR Centre for Interdisciplinary Sciences, Hyderabad. S. R. acknowledges support from the Tata Education and Development Trust and from a J C Bose Fellowship of the SERB, India. We thank R. Govindarajan for discussions. The experimental work at UMass was supported through NSF DMR-1507650.

[1] G. G. Stokes, On the effect of the internal friction of fluids on the motion of pendulums, Trans. Cambridge Philos. Soc. **IX**, 8 (1851).
[2] J. Happel and H. Brenner, *Low Reynolds Number Hydrodynamics: With Special Applications to Particulate Media* (Kluwer Publishers, Dordrecht, 1983), Vol. 1.
[3] S. Kim and S. J. Karrila, *Microhydrodynamics: Principles and Selected Applications* (Dover Publications, Boston, 1991).
[4] J. F. Brady and G. Bossis, Stokesian dynamics, Annu. Rev. Fluid Mech. **20**, 111 (1988).
[5] J.-Z. Xue, E. Herbolzheimer, M. A. Rutgers, W. B. Russel, and P. M. Chaikin, Diffusion, Dispersion, and Settling of Hard Spheres, Phys. Rev. Lett. **69**, 1715 (1992).
[6] S. Ramaswamy, Issues in the statistical mechanics of steady sedimentation, Adv. Phys. **50**, 297 (2001).
[7] I. M. Jánosi, T. Tél, D. Wolf, and J. Gallas, Chaotic particle dynamics in viscous flows: The three-particle Stokeslet problem, Phys. Rev. E **56**, 2858 (1997).
[8] M. L. Ekiel-Jeżewska, and B. U. Felderhof, Periodic sedimentation of three particles in periodic boundary conditions, Phys. Fluids **17**, 093102 (2005).
[9] É. Guazzelli and J. Hinch, Fluctuations and instability in sedimentation, Annu. Rev. Fluid Mech. **43**, 97 (2011).
[10] T. Goldfriend, H. Diamant, and T. A. Witten, Screening, Hyperuniformity, and Instability in the Sedimentation of Irregular Objects, Phys. Rev. Lett. **118**, 158005 (2017).
[11] K. V. Kumar, Ph.D. thesis, Indian Institute of Science, 2010.
[12] M. Stimson and G. B. Jeffery, The motion of two spheres in a viscous fluid, Proc. R. Soc. A **111**, 110 (1926).
[13] J. M. Crowley, Viscosity-induced instability of a one-dimensional lattice of falling spheres, J. Fluid Mech. **45**, 151 (1971).
[14] R. Lahiri and S. Ramaswamy, Are Steadily Moving Crystals Unstable?, Phys. Rev. Lett. **79**, 1150 (1997).
[15] G. B. Jeffery, The motion of ellipsoidal particles immersed in a viscous fluid, Proc. R. Soc. A **102**, 161 (1922).
[16] S. Jung, S. E. Spagnolie, K. Parikh, M. Shelley, and A. K. Tornberg, Periodic sedimentation in a Stokesian fluid, Phys. Rev. E **74**, 035302(R) (2006).
[17] T. Goldfriend, H. Diamant, and T. A. Witten, Hydrodynamic interactions between two forced objects of arbitrary shape. I. Effect on alignment, Phys. Fluids **27**, 123303 (2015).
[18] S. Wakiya, Mutual interaction of two spheroids sedimenting in a viscous fluid, J. Phys. Soc. Jpn. **20**, 1502 (1965).
[19] D. L. Koch and E. S. G. Shaqfeh, Screening in sedimenting suspensions, J. Fluid Mech. **224**, 275 (1991).
[20] A. J. Levine, S. Ramaswamy, E. Frey, and R. Bruinsma, Screened and Unscreened Phases in Sedimenting Suspensions, Phys. Rev. Lett. **81**, 5944 (1998).
[21] R. E. Caflisch and J. H. C. Luke, Variance in the sedimentation speed of a suspension, Phys. Fluids **28**, 759 (1985).
[22] See Supplemental Material at http://link.aps.org/supplemental/10.1103/PhysRevLett.122.224501 for text and videos.
[23] S. Kim, Sedimentation of two arbitrarily oriented spheroids in a viscous fluid, Int. J. Multiphase Flow **11**, 699 (1985).
[24] A. T. Chwang and T. Y. Wu, Hydromechanics of low Reynolds number flow, Part 2., J. Fluid Mech. **67**, 787 (1975).
[25] L. D. Landau and E. M. Lifshitz, *Mechanics: Course of Theoretical Physics 1* (Butterworth-Heinemann, Oxford, 2010).
[26] L. F. Shatz, Singularity method for oblate and prolate spheroids in Stokes and linearized oscillatory flow, Phys. Fluids **16**, 664 (2004).